Research Article

Heat Transfer Analysis of Nanofluid Flow on Elliptical Tube Bundle with Different Attack Angles

Amin Hosseini, Seyed Abbas Sadatsakkak *, Ali Rajabpour

Department of Mechanical Engineering, Imam Khomeini International University, Qazvin, Iran.

ABSTRACT

Flow of aluminum oxide/water nanofluid is numerically investigated in a heat exchanger at different densities of solid nanoparticles and Reynolds numbers. The behavior of heat transfer in laminar flow of single-phase nanofluid are explored at various volume fractions of oxide aluminum (0%, 2%, 4%, 6%) and Reynolds numbers (5, 15, 25, and 40) using a finite volume method. The main purpose is to study the flow behavior of nanofluid and its heat transfer in a shell and tube heat exchanger with tube banks of the elliptical cross-section with different angles of attack. The results of this study indicate that an increase in the velocity of flow enhances the heat transfer coefficient, resulting in a more uniform temperature distribution. In addition, increase of angle of attack leads to a higher velocity of the fluid flow between the tubes. At higher Reynolds numbers, more remarkable entropy reduction is observed with increasing nanoparticle volume fraction. Depending on its volume fraction, addition of solid nanoparticles at a constant Reynolds number amplifies the flow velocity components and reduces the temperature gradient. The Nusselt number can increase up to 17% in Reynolds number of 5 for all tube banks depending on the volume fraction and angle of attack, which is up to 23% for Re = 40. Therefore, the amount of shell-side friction coefficient increases by 25 to 35% for Re = 5 to 40. For all designs, the increase in the friction coefficient due to angle of attack is less important than the variations of nanofluid volume fractions.

1. Introduction

Nowadays, heat exchangers are extensively used in various fields such as boilers, steam generators, condensers, evaporators, cooling towers of power plants, fan coils, preheaters, and oil coolers. Therefore, methods to improve the performance of heat exchangers are of crucial significance and priority for designers. The finned surfaces, new cooling substrates or nanofluids with improved rheological properties, and non-circular sections have been applied as effective approaches in heat transfer industries. The adoption of new methods in heat transfer tools such as heat exchangers and changing dimensions and geometric arrangement can be an effective and beneficial method which requires further research. In this regard, researchers have conducted many studies to experimentally and numerically investigate the flow on the tube banks. Bahiraei et al. [1] explored the effect of using common nanofluids with water base fluid or in some limited cases ethylene glycol with various nanoparticles (NPs) (e.g. Al_2O_3, CeO_2, TiO_2, Ag, $MWCNT$, CNT, Cu, CuO, SiO_2, Fe_2O_3, ZnO, Fe_3O_4, MgO, MgO and graphene) on the performance of heat exchangers. Their results showed that the presence of solid nanoparticles (NPs) can improve heat transfer and flow properties. The optimization of nanofluid-containing two-tube heat exchangers with elliptical cross-section was numerically achieved by Khan

Corresponding Author: Seyed Abbas Sadatsakkak
Email: sakak@eng.ikiu.ac.ir

Mohammadi et al. [2]. Their results indicated that changes in Nusselt number, friction coefficient, and entropy depend on the content of solid NPs, Reynolds number (Re), and the spiral diameter. Tang et al. [3] examined longitudinal vortex generators on the tube bank with elliptical cross-section in the presence of air fluid. They showed that the use of the vortex-generating vanes on the tube bank increases the efficiency of the heat exchanger Zhao et al. [4] investigated the effects of the arrangement of elliptical tubes in a horizontal heat exchanger and the heat transfer in the presence of air fluid. Three states were addressed, where the tubes were in rows and columns below each other, in a half-step column, and half a step apart in row state. Their results indicated that each structure has its own characteristics which can affect heat transfer and friction coefficient. Deepakumar and Jayaval [5] evaluated the effects of different arrangements of circular and elliptical tubes on heat transfer parameters and pressure drop in a multi-row finned tube heat exchanger in the presence of air. Their results showed higher thermal efficiency when circular tubes are placed first followed by elliptical tubes in the flow path. Saffarian et al. [6] numerically assessed shell and tube heat exchangers with different types of tubes. Their results indicated that the pressure drop in elliptical tubes is 90 degrees higher than circular tubes; they also reported higher heat transfer in the elliptical tubes. Therefore, the shape of the cross-section of the tubes and their location in the shell and in the core can significantly affect the pressure drop. The flow and friction coefficient of air fluid in cam-shaped tube bank was numerically explored in the Reynolds number range of 11500 to 42500 Mangrulkar et al. [7]. Their results showed higher thermal efficiency of fluids in tube bank with a cam section compared to a tube bank with a circular section. In the mentioned type of section, the friction coefficient is reduced by 85-89% compared to the circular section. Wu et al. [8] evaluated the parameters of heat transfer and flow in twisted elliptical tube with an elliptical cross-section in the presence of air. According to their results, compared to elliptical tube, the use of a twisted elliptical tube increases the Nusselt number and pressure drop by 16-19% and 58-60%, respectively. Etaig and Hashem [9] numerically investigated the laminar flow in a vertical tube with elliptical cross section. In this research, numerical simulation was used to model the heat transfer and flow characteristics in an elliptical tube. Their results indicated a significant increase in the heat transfer and the shell friction coefficient with the increment of the Reynolds number. The heat transfer coefficient at the flow input was the maximum value and gradually decreased along the length of the channel. Lu and Zhai [10] investigated the effect of vortex generator vanes on elliptical tubes on heat transfer and flow parameters of a heat exchanger with airflow. Their

results showed that the use of vortex generator vanes increases the overall performance coefficient. Akbari et al. [11] explored the flow of nanofluid in a 3-D curved microtube. They found somewhat distinct characteristics, hydrodynamic behavior, and heat transfer of nanofluid in circular geometries due to the existence of buoyancy and centrifugal forces caused by the geometric shape, compared to other geometries and panplane, such that the movement of the nanofluid in the zones before and after a 45-degree twist of the microtube caused unpredictable changes in the hydrodynamic and heat transfer parameters. Mousavi et al. [12] examined the heat transfer and forced flow of copper water nanofluid on elliptical tube banks and evaluated the flow and heat transfer behavior in different arrangements and different volume fractions. Their results indicated better fusion in the RS configuration, due to the separation of the flow which significantly enhanced the local Nusselt number. Liu et al. [13] assessed flow parameters and heat transfer in a rectangular channel with combined delta winglet inserts in the presence of air. They numerically and experimentally investigated the flow and heat transfer parameters for 4 different arrangements of delta vanes, the space between the delta vanes, the connection center of the delta vanes, and the angle of rotation of the delta vanes. Mangrulkar et al. [14] numerically and experimentally evaluated the flow of air fluid on the tube bank with the integral splitter plate in the Reynolds number range of 5500-14500. Their results showed an increment in the Nusselt number for the fluid flow upon the use of a splitter plate in the tube sequence. Moreover, the use of the integral plate enhanced the heat transfer and thermal-fluidic efficiency by reducing the pressure drop compared to the normal tube bank. The maximum increase of the thermal fluidic performance was 60-82% for Re=5500. To improve fluid flow and heat transfer behavior in shell and tube heat exchangers with continuous spiral baffles, Arani and Uosofvand [15] investigated the variations of horizontal and vertical positions for different angles of elliptical tubes and showed that the performance of heat exchangers is significantly influenced by the tube pattern. Pourfattah et al. [16] numerically investigated the turbulent flow of water/alumina nanofluid in a tube with inclined cogs at different angles of attack. Their numerical results indicated an increase in the heat transfer upon raising the volume fraction of solid nanoparticles and the attack angle of the cogs.

Regarding the extensive recent investigations, numerous studies have addressed the heat transfer in heat exchangers with different structures of tube banks, type of exchanger, and nanofluids (with various aspect ratios). On the other hand, heat transfer in heat exchangers has been a hot topic in research communities and the industry sector. Heat exchangers can be regarded as the most widely used tool in

chemical processes as well as industrial units and power plants where the issue of heat transfer is important. These applications include power plants, refineries, petrochemical industries, manufacturing and manufacturing industries, process industries, food and medicine, metal smelting, heating, air conditioning, refrigeration systems, and aerospace.

The use of the heat exchanger with elliptical tube bank of various angles of attack has not been addressed a lot. In this numerical research, the flow and laminar heat transfer of water/alumina nanofluid are simulated on tube banks with an elliptical cross-section at different angles of attack. The main purpose of this study is to determine the flow parameters and heat transfer for various angles of attack (0°-90°). For this purpose, the results of the present research will be drawn and compared in terms of Nusselt number, friction coefficient, production entropy and temperature, and flow field for a laminar nanofluid flow.

2. Problem Statement

This research presents the numerical simulation of the flow and laminar and forced heat transfer of water/aluminum oxide nanofluid on tube banks with elliptical cross-section for different angles of attack (if a horizontal line is drawn in the direction of the fluid flow, the degree of rotation of the pipe handle in the vertical direction or the change of the position of the pipe handle, the angle of attack of the pipe handle is defined) in a single-phase heat exchanger. The square geometry of the tube banks is depicted in Figure 1. As seen, the dimensions of the defined geometry include the inlet length L_{us}, the middle length L_{tb}, the outlet length L_{ds} and d the equivalent or hydraulic diameter of the tube with an elliptical section (for elliptical tube banks D=6 cm and d=3 cm). In this simulation, the diameter of the tube is equal to D_h=3.79cm and the length of the input area is determined as L_{us}=50cm, L_{ds}=30cm, and L_{tb}=40cm. The behavior of heat transfer and laminar flow of single-phase nanofluid are explored at various volume fractions of solid aluminum NPs (0%, 2%, 4%, 6%) and Reynolds numbers (5, 15, 25, and 40) using a finite volume method. The rows of tube bundles will be divided as R1, R2, and R3 in the description of the results.
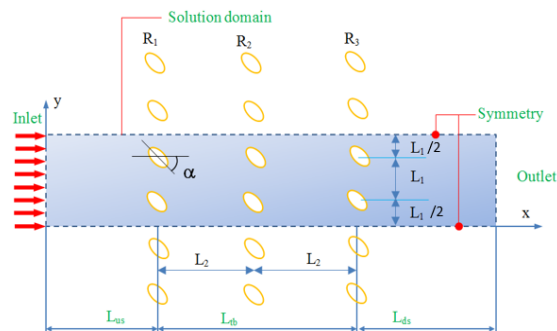

Figure 1. Schematic of the studied geometry

The temperature of the tube wall is T=308 K while the temperature of the inlet fluid is taken 293 K. The diameter of solid nanoparticles is 10 nm. Aluminum nanoparticles and water base fluid are considered according to Table 1. [17]

Table 1. Thermo-physical properties of base fluid and solid NPs

	AL_2O_3	Water
$\rho \left(Kg \text{ m}^{-3} \right)$	3970	997.1
$k \left(\text{W m}^{-1} \text{ K}^{-1} \right)$	40	0.613
$C_p \left(\text{J Kg}^{-1} \text{ K}^{-1} \right)$	765	4179
$\mu \left(\text{Pa s} \right)$	-	0.000891

Although there are different methods for modeling fluid flow and heat transfer in heat exchangers, this research is generalized to the finite volume method with the help of computer code in two-dimensional space. The purpose of this research is to investigate and compare the heat transfer and flow of single-phase nanofluid in the tube bank. Here, the nanofluid flow is laminar and forced, single-phase, and Newtonian, neglecting the effects of radiation. The governing equations of the single-phase and laminar flow of nanofluids include continuity equations, momentum equations, and energy equations.

In the continuation of this research, the expression and introduction of the governing equations to solve the problem will be presented.

3. Governing Equations

The governing equations including the continuity, momentum, and energy equations are solved in Cartesian coordinates for steady and laminar states [18].

Continuity equation:

$$\frac{\partial \text{u}}{\partial \text{x}} + \frac{\partial \text{v}}{\partial \text{y}} = 0 \tag{1}$$

Momentum equations:

$$\text{u} \frac{\partial \text{v}}{\partial \text{x}} + \text{v} \frac{\partial \text{v}}{\partial \text{y}} =$$
$$-\frac{1}{\rho_{\text{nf}}} \frac{\partial \text{p}}{\partial \text{y}} + \nu_{\text{nf}} \left(\frac{\partial}{\partial \text{x}} \left(\frac{\partial \text{v}}{\partial \text{x}} \right) + \frac{\partial}{\partial \text{y}} \left(\frac{\partial \text{v}}{\partial \text{y}} \right) \right) \tag{2}$$

$$\text{u} \frac{\partial \text{u}}{\partial \text{x}} + \text{v} \frac{\partial \text{u}}{\partial \text{y}} =$$
$$-\frac{1}{\rho_{\text{nf}}} \frac{\partial \text{p}}{\partial \text{x}} + \nu_{\text{nf}} \left(\frac{\partial}{\partial \text{x}} \left(\frac{\partial \text{u}}{\partial \text{x}} \right) + \frac{\partial}{\partial \text{y}} \left(\frac{\partial \text{u}}{\partial \text{y}} \right) \right) \tag{3}$$

Energy equation:

$$u\frac{\partial T}{\partial x} + v\frac{\partial T}{\partial y} =$$
$$\frac{1}{C_{p_{nf}}\rho_{nf}}\left(\frac{\partial}{\partial x}\left(k_{nf}\frac{\partial T}{\partial x}\right) + \frac{\partial}{\partial y}\left(k_{nf}\frac{\partial T}{\partial y}\right)\right) \quad (4)$$

The following definitions are used to obtain non-dimensional parameters [19].

$$X = \frac{x}{d} \qquad\qquad \theta = \frac{T - T_c}{\Delta T} \quad (5)$$

The following relations are used to calculate the density, effective dynamic viscosity, and specific heat capacity of nanofluid (20-22):

$$\rho_{nf} = (1 - \varphi)\rho_f + \varphi\rho_s \quad (6)$$

$$\mu_{nf} = \frac{\mu_f}{(1 - \varphi)^{2.5}} \quad (7)$$

$$(\rho C_p)_{nf} = (1 - \varphi)(\rho C_p)_f + \varphi(\rho C_p)_s \quad (8)$$

The Patel et al.'s equation is employed to calculate the effective thermal conductivity coefficient of suspensions containing spherical particles [23].

$$k_{eff} = k_f\left[1 + \frac{k_s A_s}{k_f A_f} + ck_s Pe\frac{A_s}{k_f A_f}\right] \quad (9)$$

In which, c=36000.

$$\frac{A_s}{A_f} = \frac{d_f}{d_s}\frac{\varphi}{1 - \varphi} \quad (10)$$

$$Pe = \frac{u_s d_s}{\alpha_f} \quad (11)$$

In Eqs. (10) and (11), the diameter of the water molecule is equal to d_f = 2Å while the diameter of the Al$_2$O$_3$ nanoparticle molecule is taken d_s= 50 nm. The velocity of the Brownian motion of the nanoparticles, u_s, can be determined by the following equation [24-25]:

$$u_s = \frac{2\kappa_b T}{\pi\mu_f d_s^2} \quad (12)$$

In Eq. (12), K_b is Boltzmann's constant (1.3807 × 10^{-23}J/K). The following equation is also used to calculate the average Nusselt number along the tube walls [26].

$$Nu_{ave} = \frac{h\,d}{k_f} \quad (13)$$

The friction factor is another parameter for investigating the performance of microchannel, which is calculated as [27].

$$Cf = \frac{2 \times \tau_w}{\rho u_{in}^2} \quad (14)$$

The pressure drop coefficient can be obtained by the following equation [12]:

$$Cp = \frac{P - P_{out}}{\frac{1}{2} \times \rho \times u^2} \quad (15)$$

The pressure drop at the inlet and outlet sections can be determined by [12]:

$$\Delta P = \overline{P}_{out} - \overline{P}_{in} \quad (16)$$

Reynolds numbers are calculated based on the diameter of tube banks [28]:

$$Re = \frac{\rho \times d \times u_{in}}{\mu} \quad (17)$$

The entropy generated due to thermal irreversibility (heat transfer) and friction coefficient is equal to [29, 30],

$$S_{gen} = \frac{k_{eff}}{\overline{T}^2}\left[\left(\frac{\partial\overline{T}}{\partial x}\right)^2 + \left(\frac{\partial\overline{T}}{\partial y}\right)^2\right] \quad (18)$$

$$S_{gen} = \frac{\mu_{eff}}{\overline{T}}\left\{2\left[\left(\frac{\partial\overline{u}}{\partial x}\right)^2 + \left(\frac{\partial\overline{v}}{\partial y}\right)^2\right] + \left(\frac{\partial\overline{u}}{\partial x} + \frac{\partial\overline{v}}{\partial y}\right)^2\right\} \quad (19)$$

The amount of total entropy, which includes the increase in entropy due to heat transfer and flow friction, is calculated from the following equation [31,32].

$$S_{gen} = \frac{k_{eff}}{\overline{T}^2}\left[\left(\frac{\partial\overline{T}}{\partial x}\right)^2 + \left(\frac{\partial\overline{T}}{\partial y}\right)^2\right]$$
$$+ \frac{\mu_{eff}}{\overline{T}}\left\{2\left[\left(\frac{\partial\overline{u}}{\partial x}\right)^2 + \left(\frac{\partial\overline{v}}{\partial y}\right)^2\right] + \left(\frac{\partial\overline{u}}{\partial x} + \frac{\partial\overline{v}}{\partial y}\right)^2\right\} \quad (20)$$

4. Numerical Solution, Network Independence, and Assumptions

According to figure 2, triangular mesh is used in this research. In order to increase the accuracy and reduce the numerical error and estimate the flow behavior in the areas close to the wall, fine meshes have been used in the areas close to the bundle of tubes. To verify the obtained results, the number of meshes was changed from 9000 to 81000 grids as listed in Table 2. Then,

heat transfer parameters such as Nusselt number and hydrodynamic parameters of friction coefficient were examined. Accordingly, the parameters of the friction coefficient and the average Nusselt number on the hot wall of the first tube bank can be obtained with an Error< 2% for 81000 grids. Meanwhile, selecting fewer grids can save time and computational costs.

Table 2. The mesh-independence of numerical results

Mesh Size (x,y)	Nu	F
9000	7.108	0.695
16000	7.13	0.681
25000	8.138	0.673
56250	9.121	0.6621
68000	9.67	0.6501
81000	9.96	0.626
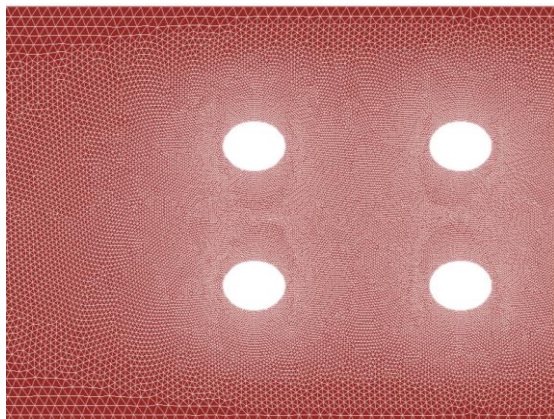
Figure 2. The figure of the mesh structure

The finite volume method was employed for simulation. A simple algorithm was adopted for the connection between pressure and velocity field. All equations were discretized by the second-order upwind method while a standard method was used for compressive interpolation. The flow in the heat exchanger is assumed to be laminar, Newtonian, single-phase, and incompressible. No-slip boundary condition is considered at the walls. Radiation effects are negligible. In the simulation, the nanofluid is assumed to be homogeneous.

5.   Discussion and Providing the Results

5.1.   Validation

The present study was validated by comparison with the numerical results of Mousavi et al. [12] for pure water with the Reynolds number of 100 in the arrangement of the tube bank with the ES model as depicted in Figure 3. In this research, alteration of the Nusselt number on the hot surface of the tube bank was recreated separately for different rows of the tube bank. Mousavi et al. [12] investigated the flow

structure and heat transfer on the elliptical tube banks with different arrangements and Reynolds numbers (100-700). Nanofluid was utilized to increase the thermal performance of the heat exchanger. The results and their quantitative comparison confirmed the boundary conditions and presuppositions with negligible error.
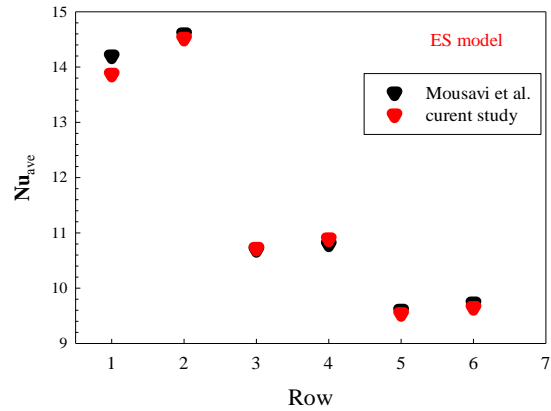
Figure 3. Validation of the results of the present research with the work of Mousavi et al. [12]

5.2.   Contours of Dimensionless Temperature Distribution

The dimensionless temperature distribution contours are presented in Figure 4 at various angles of attack (0°-90°) for different Reynolds numbers. Figure 4 also depicts the dimensionless temperature at various angles of attack (0°-90°) and Reynolds numbers (5-40). Upon the entrance of the flow into the tube banks heat transfer occurs due to the temperature difference between the fluid and the tube surface. Regarding the spiral paths, a thermal boundary layer is formed. At Re=5, the temperature variations and temperature gradients are increased due to the slower movement of the fluid, which enhances the facade and colored zones. At Re=40, the temperature changes are lower because of the higher fluid velocity and greater heat transfer between the surface and the fluid, therefore, the cooling of the tube banks will be higher and the temperature gradients are more limited compared to Re=5 according to the coloring. An increment in the flow velocity enhances the convective heat transfer coefficient rises due to the higher Reynolds number, which will lead to a more uniform temperature distribution and lower temperature gradients. On the other hand, changes in the angle of attack can move the flow. The fluid with various angles of attack flows between the tube banks which can affect the flow rate. According to the contours in Figure 4, variations of the angle of attack alter the temperature gradients, especially in the zones behind the tubes. At zero angle of attack, the fluid moves easily because of the insignificant angle of attack of the flow in contact with the fluid, The zone behind the tubes is

associated with smaller gradients. By raising the angle of attack by 90°, the temperature alterations are remarkable and cover a larger area as the flow is associated with high velocity gradients after passing through the tube banks.

The contours of Figure 5 compare the variations of dimensionless temperature distribution in different contents of solid nanoparticles (0%, 2%, 4%, and 6%) and Reynolds numbers (5-40). The presence of solid NPs in the cooling fluid increases the thermal conductivity of the cooling fluid, improving the thermal conductivity and leading to more uniform heat

distribution. According to Figure 5, an increase in the volume fraction of nanoparticles is associated with lower gradients. Moreover, the incorporation of higher contents of solid nanoparticles at Re=40 will more effectively reduce the temperature gradients due to the enhancement of the flow velocity. Thus, the effectiveness of nanofluid at Re=5 is less dependent on the volume fraction and this behavior is more effective at Re=40. Therefore, the incorporation of higher amounts of solid nanoparticles at high Reynolds numbers and fluid velocities can more effectively limit the temperature gradients.
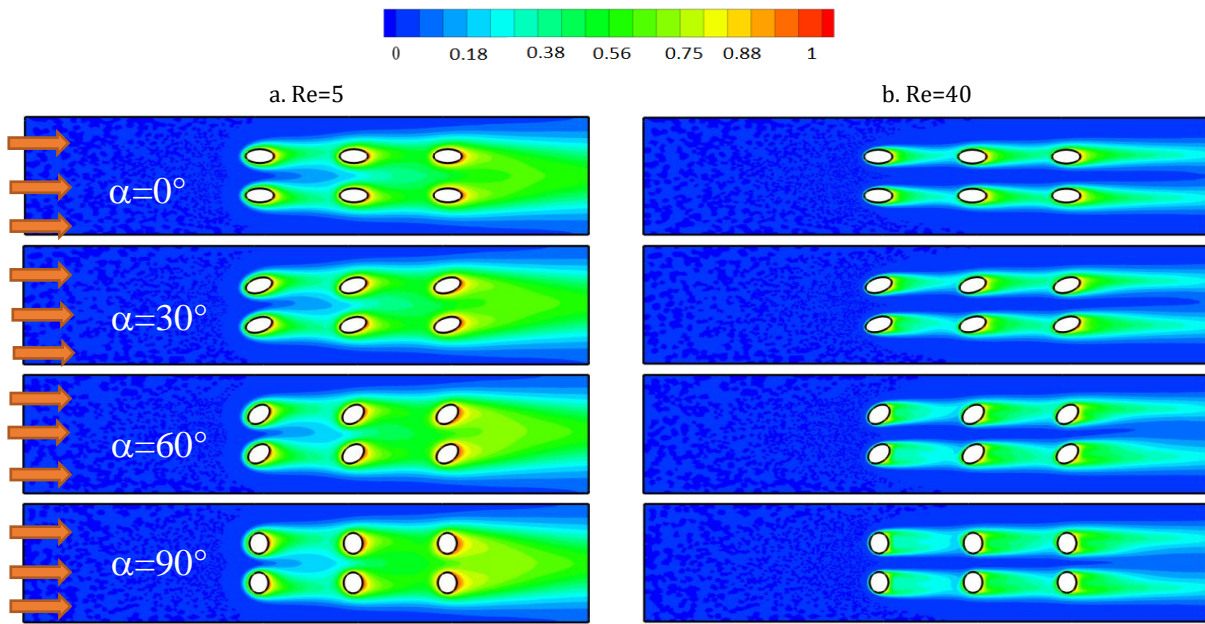

Figure 4. Dimensionless temperature distribution contours at different angles of attack and Reynolds numbers
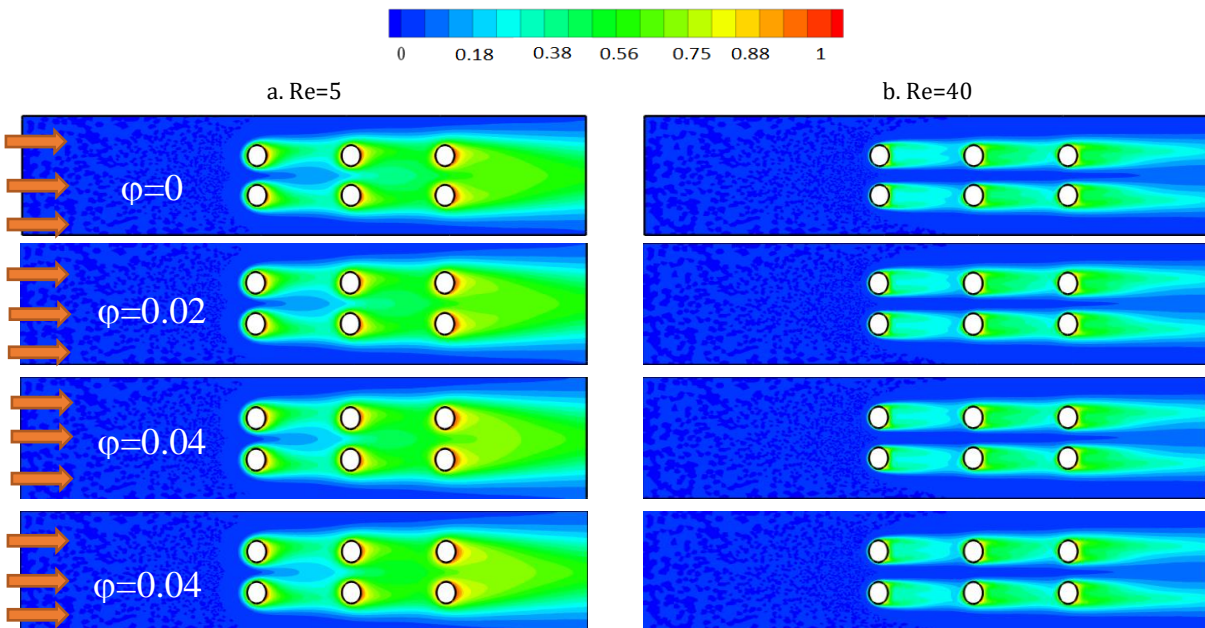

Figure 5. Dimensionless temperature distribution contours for different solid nanoparticle volume fractions and Reynolds numbers (5 and 40)

5.3. Entropy Distribution Contours

The contours in Figure 6 show the distribution of local entropy at different angles of attack and Reynold numbers. Re=5 is associated with higher temperature gradients due to the limited fluid velocity. Regarding the lower fluid velocity, temperature gradient increases due to the slower movement of the fluid. When the cold fluid moves, it is associated with a higher heat transfer due to the fact that it can maintain the temperature difference along its path, thus, the temperature gradient is reduced, declining the produced entropy. Moreover, the presence of a tube bank with a greater angle of attack can result in a larger separation zone at the back of the tubes due to the separation of the fluid from the surface. Therefore, lower heat transfer occurs, leading to the formation of hot zones with higher temperatures. This will enhance the entropy behind the tube banks at a higher angle of attack. At higher Reynolds numbers, the heat transfer coefficient increases and the temperature distribution gets uniform due to the strengthening of the fluid velocity components which can lower the temperature gradients and decrease the production entropy.

Figure 7 shows the contours of entropy production for different contents of solid nanoparticle and Reynolds numbers (5 and 40). The presence of solid nanoparticle in the cooling fluid leads to uniform temperature distribution which can significantly reduce the entropy production due to temperature gradients. Furthermore, the presence of solid NPs at Re=40 results in significant changes and higher entropy reduction rates. Regarding the changes in the volume fraction of solid NPs at Re=5 and 40, the addition of solid NPs in higher Reynolds numbers leads to more significant reduction of entropy. At Re=5, changes of entropy by content of NPs are more limited.
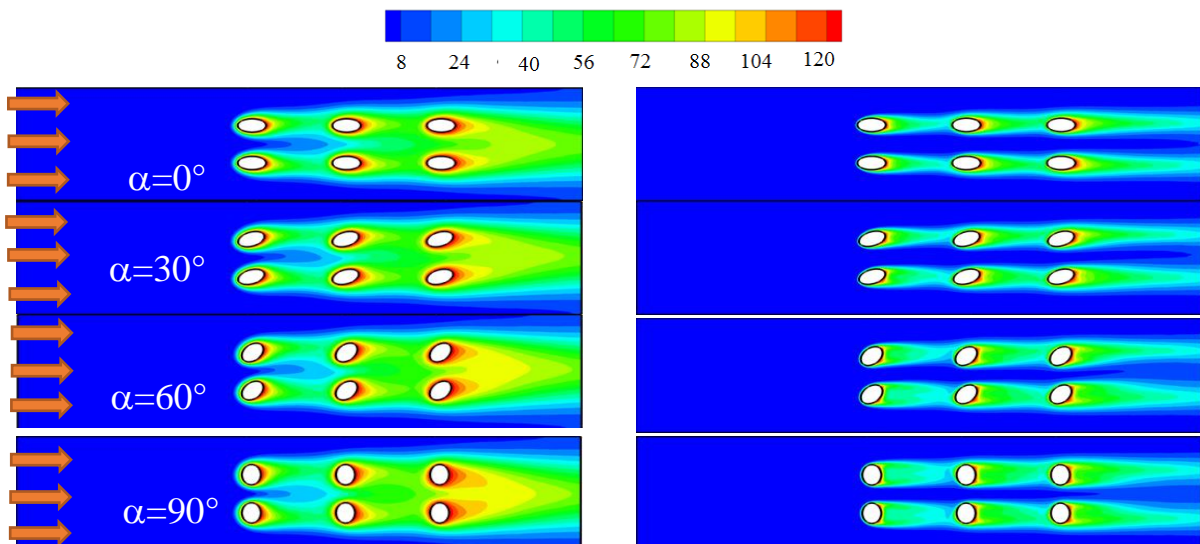

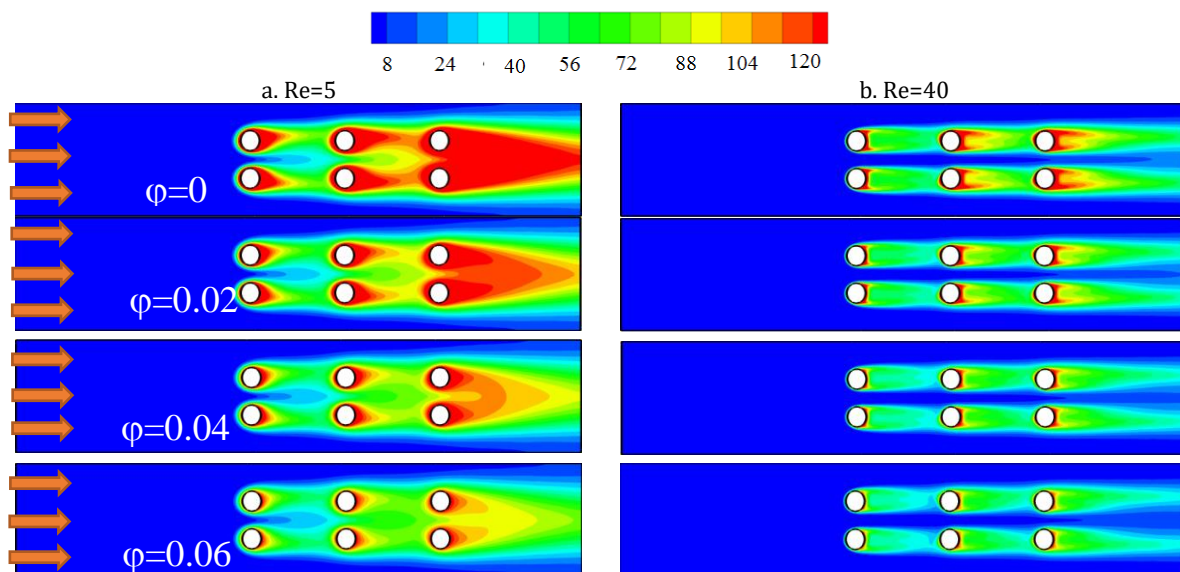**Figure 6.** Contours of entropy distribution at different angles of attack and Reynolds number

Figure 7. Entropy produced at different volume fractions of solid nanoparticles and Reynolds numbers of 5 and 40

5.4. Nusselt Number Diagrams

Figure 8 compares the graphs of average Nusselt number for various volume fractions of NPs, angles of attack (0°, 30°, 60°, and 90°), and Reynolds number. In this study, tube banks 1-3 are compared with each other. In all the graphs, the increase in the Reynolds number enhanced the Nusselt number due to the rise in the fluid velocity [33-35]. Thus, the presence of solid nanoparticles increased the Nusselt number and improved heat transfer due to the enhancement of the thermal conductivity of the cooling fluid. In all the graphs, the Nusselt number graphs showed a

significantly ascending trend by increasing the angle of attack of the tube banks, due to the impact of the flow on the surface of the heating zone. The highest value of Nusselt number is related to R1, R2, and R3 with lower heat transfer. The first contact of the fluid with the tube bank, which takes place at R1, is associated with the highest amount of heat transfer, due to the maximum temperature difference between the surface and the fluid. In the next tubes, the behavior of the Nusselt number at R2 and R3 are close together as the heat transfer occurs before the collision of fluid with R2 and R3, hence, the temperature difference and the heating rate of the fluid will be decreased.
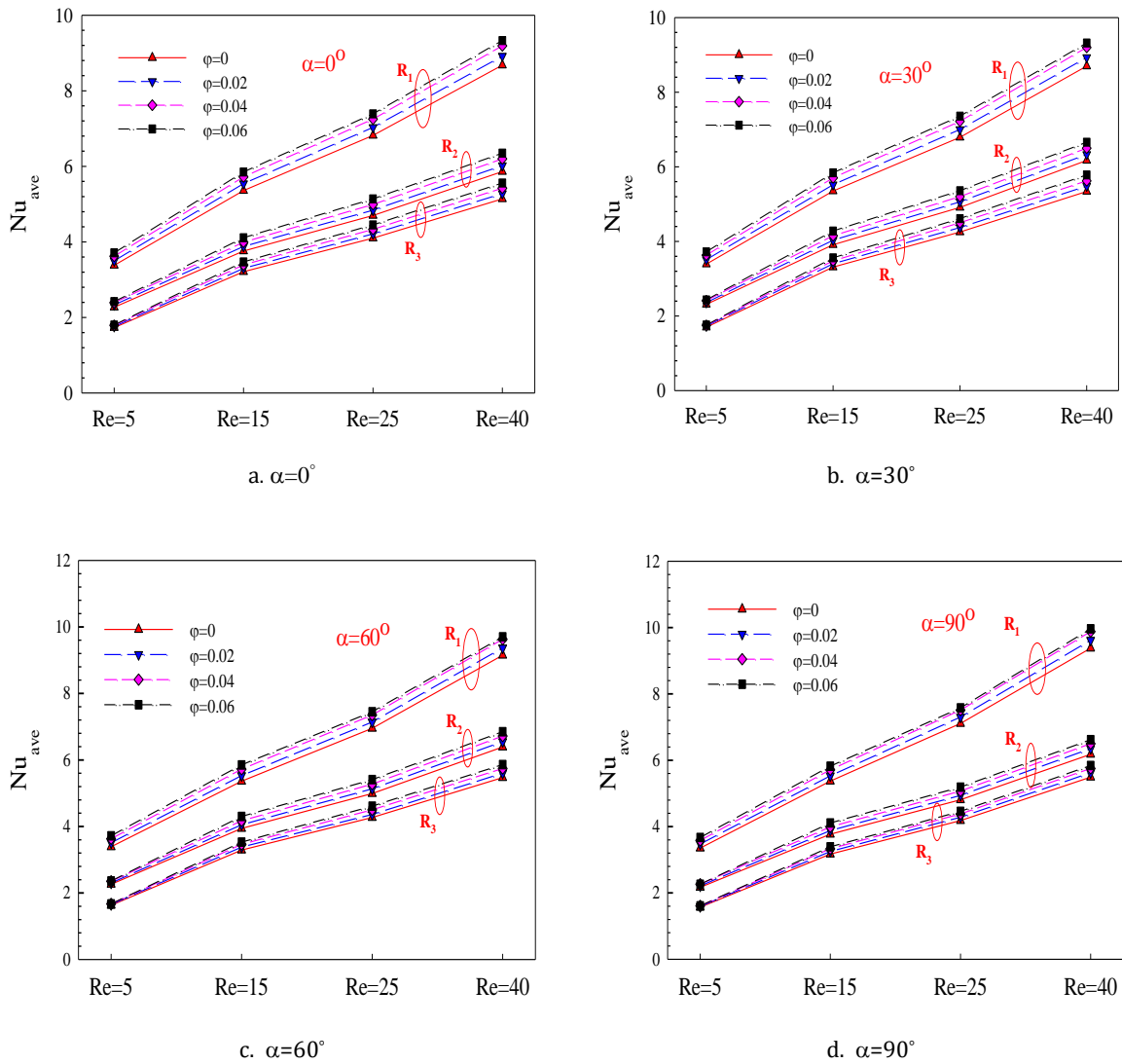

a. α=0°

b. α=30°

c. α=60°

d. α=90°

Figure 8. Average Nusselt number for different volume fractions of NPs, angles of attack, and Reynolds number

5.5. Heat Flux Diagrams

Figure 9 depicts the distribution of average surface heat flux vs. NPs volume fraction, angle of attack, and Reynolds number (5-40) for different tube banks. Figure 8 thus compares the changes in the heat flux absorbed by the fluid on the hot surface of the tube banks (R1 to R3) for diverse NPs volume fractions, Reynolds numbers, and angles of attack (0°, 30°, 60°, and 90°). Any factor capable of increasing the heat transfer can increment the surface-absorbed heat flux. The presence of solid nanoparticles, the increase in the Reynolds number, and a rise in the angle of attack can increase the heat flux absorbed from the tuba banks. Therefore, the value of heat flux absorbed from tube bank 1 can increase heat transfer by twice and four times compared to tube banks 2 and 3, respectively.
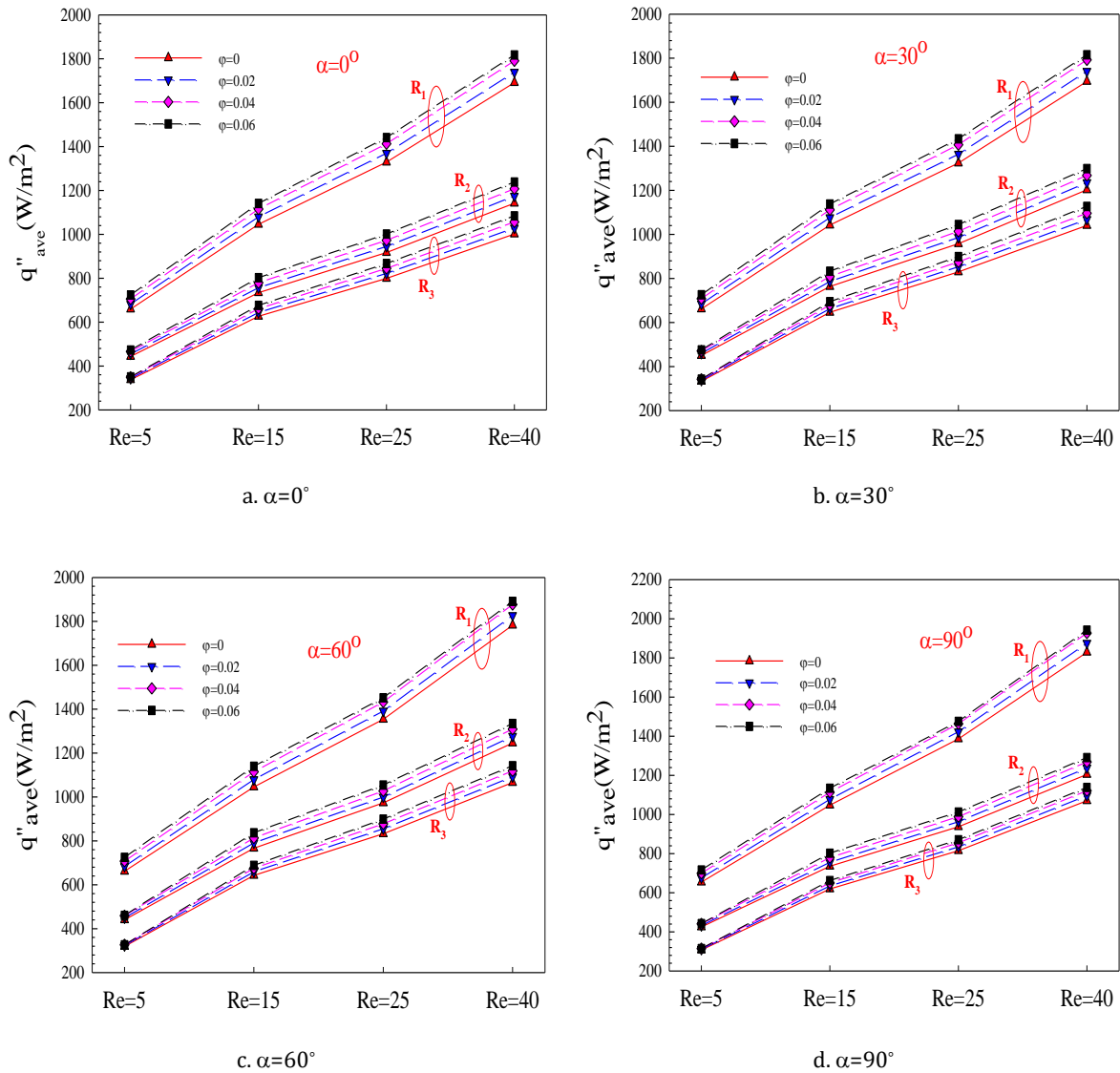

a. α=0˚

b. α=30˚

c. α=60˚

d. α=90˚

Figure 9. Average surface heat flux distribution for different NPs volume fraction, angles of attack, and Reynolds numbers (5-40)

5.6. Diagrams of Dynamic Pressure Drop Coefficient

Figure 10 presents the dynamic pressure drop coefficient for different NPs volume fractions, angles of attack, and Reynolds numbers (5-40) in the tube banks 1 and 3. At Re=5, the momentum depreciation rate is higher upon collision with the surface of the tube bank due to the lower velocity of the fluid. Moreover, a large part of the fluid velocity is reduced and the flow components are associated with higher depreciation due to the impact of the flow on the tube banks. The dynamic pressure drop also exhibits an increment. At higher Reynolds numbers, the dynamic pressure drop decreases due to the strengthening of the fluid momentum and lower changes in the flow velocity components. Also, the presence of solid NPs in the cooling fluid is associated with an increase in viscosity and density. The viscous and heavier fluid requires the higher momentum to move and will exhibit high depreciation upon collision with the tuba banks. Thus, the largest dynamic pressure drop is related to the fluid containing 6 vol.% NPs in all cases. The angle of attack of the tube bank increases due to the rise in the energy absorption of the fluid. The fluid is associated with higher momentum depreciation. The pressure drop at the angle of 90° is higher than to the angles of attack of 0°, 30°, and 60°.
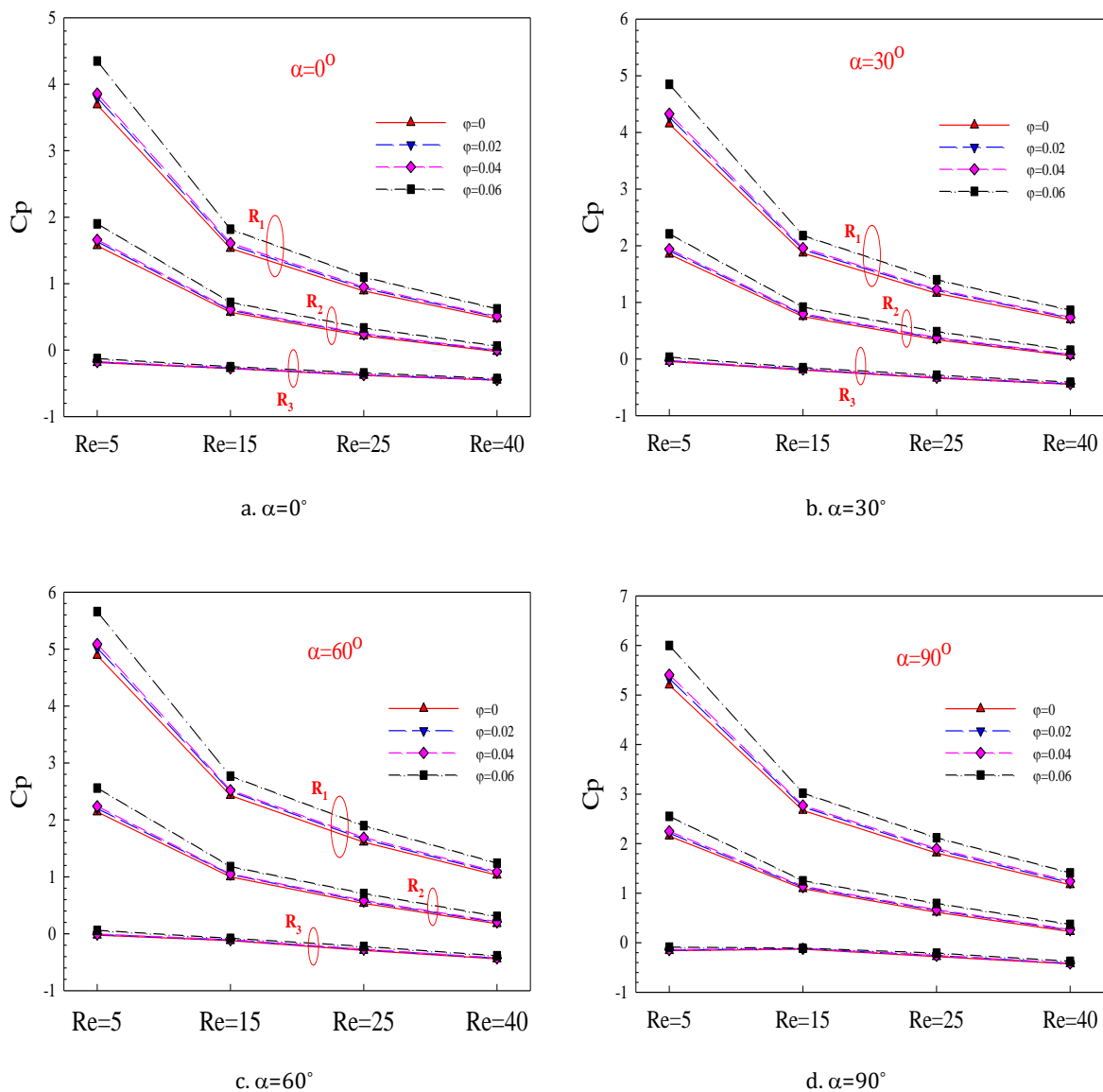
Figure 10. Dynamic pressure drop coefficient for various NPs volume fraction, angles of attack and Reynolds numbers (5-40)

5.7. Average Entropy Generation

Figure 11 shows the changes in the average entropy generation in different tube banks for various NPs volume fractions (0%, 2%, 4%, and 6%), angles of attack, and Reynolds numbers. Entropy variations in the flow path on the tube banks are under the influence of two factors: temperature gradients and the friction coefficient created due to the flow passing over the tube banks and the zones behind them (also including the flow separation parts). Any factor capable of enhancing heat transfer can inversely affect entropy changes. In all the graphs, the entropy variations were descending with the increase of the Reynolds number due to the reduction of temperature gradients and friction coefficient. Thus, the presence of solid NPs in the tube banks leads to more uniform heat distribution, less temperature gradients, and lower entropy production, which ultimately decrements the entropy in cases. Among the reviewed graphs, the changes in the angle of attack increase the friction coefficient due to the alterations in the flow velocity components. The friction coefficient created on the tube banks is due to the flow velocity components. As the angle of attack increases, the amount of entropy produced by friction increases due to the componentization of the flow. Thus, the highest entropy generation is for tube banks No. 3 due to the rise of frictional entropy and gradients velocity, as well as an increase in temperature gradients, which enhanced entropy caused by heat and ultimately incremented the total entropy. The lowest amount of entropy production is related to the first tube bank with a minimum entropy value due to heat transfer as a result of surface-fluid temperature difference. Therefore, the lowest total average entropy is related to the first tube bank.
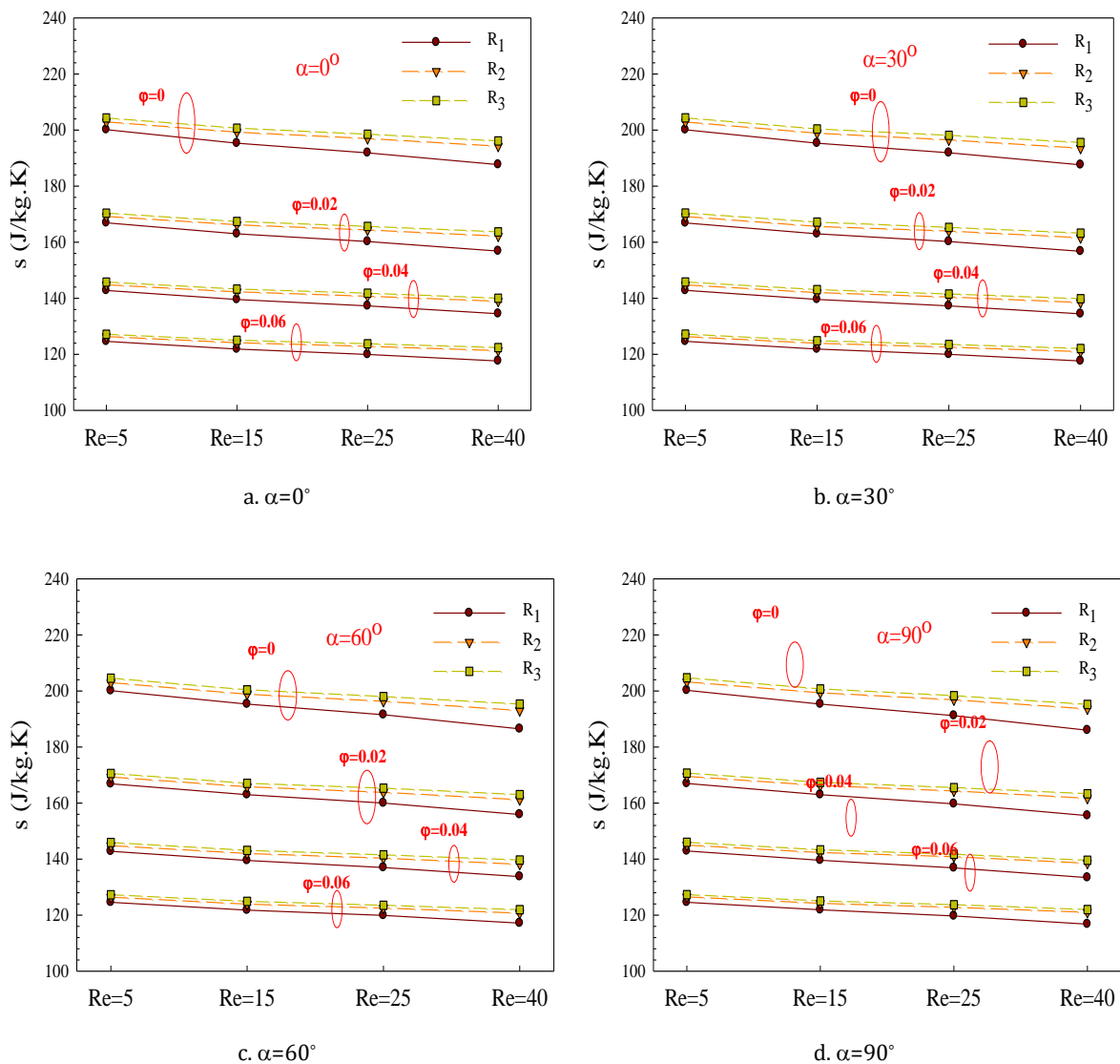

a. $\alpha=0°$

b. $\alpha=30°$

c. $\alpha=60°$

d. $\alpha=90°$

Figure 11. Average entropy generation in different tube banks for various NPs volume fractions, angles of attack, and Reynolds numbers.

5.8. Average Surface Friction Coefficient

Figure 12 illustrates the average surface friction coefficient for various NPs volume fractions (0% and 6%), angles of attack (0°-90°), and Reynolds numbers (5-40). Changes in the friction coefficient in the tube banks can be assigned to the variation of the flow path due to collision with the tube banks. Therefore, the presence of solid NPs in the cooling fluid is associated with an increase in viscosity and density. A heavier fluid with a higher viscosity requires a higher momentum to move, resulting in larger momentum consumption and greater friction coefficient. In all the graphs, the highest friction coefficient is related to the

NPs volume fraction of (6%) while the base fluid exhibits the lowest friction coefficient. Also, the friction coefficient decreased with the enhancement of the fluid velocity due to the lower flow velocity. The graphs also display a decreasing trend with the increase of the Reynolds number. Therefore, the angle of attack can affect the direction of the flow of movement, enhancing the friction coefficient. The highest friction coefficient is related to R1, R2, and R3, respectively. In the R3 zone, the collision with the tube banks occurs at lower velocities due to higher depreciation, leading to the lowest friction coefficient. The highest friction coefficient is related to R1 due to collision with the fluid in the first row.

a. $\alpha=0°$

b. $\alpha=30°$

c. $\alpha=60°$

d. $\alpha=90°$
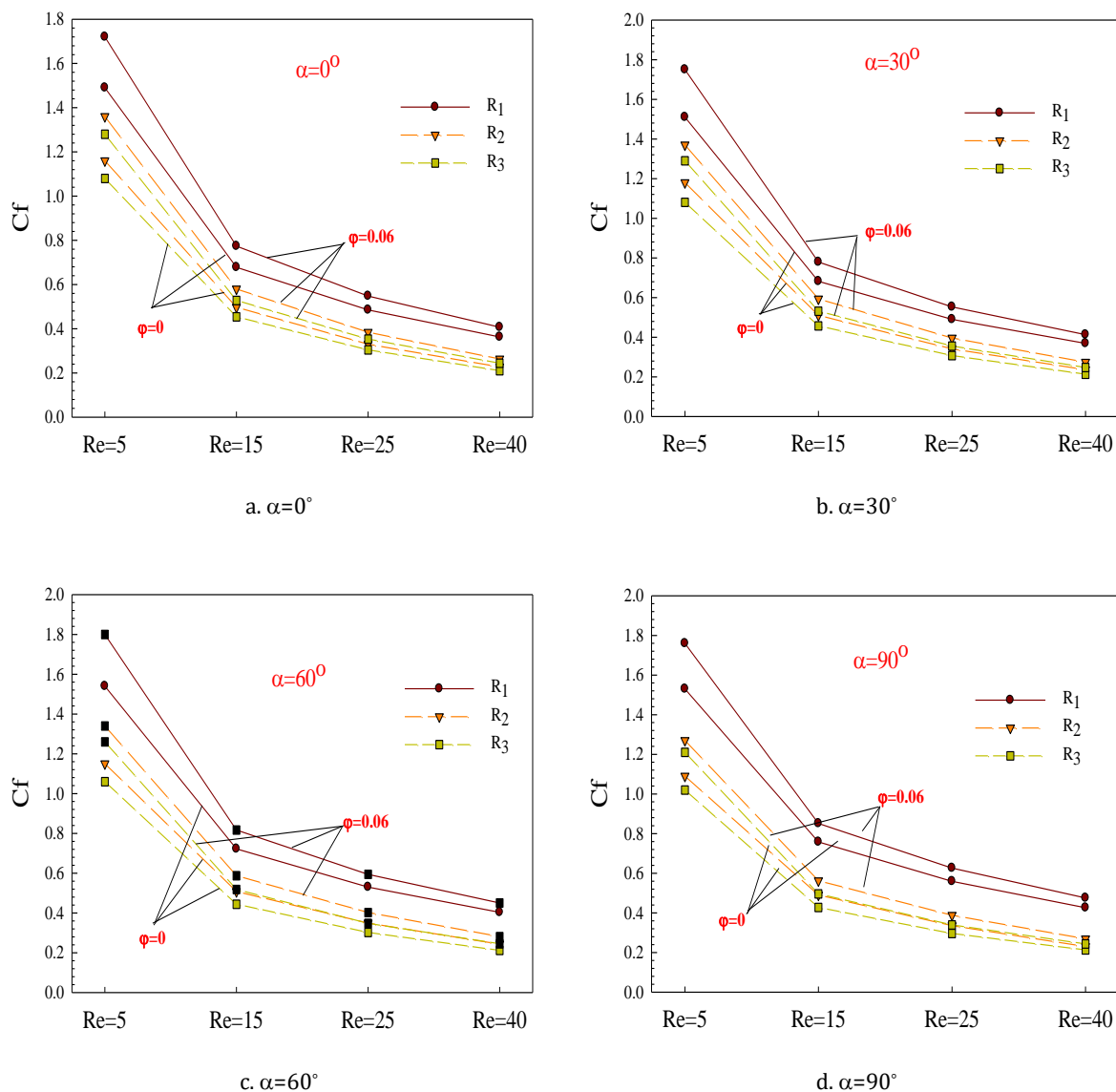
Figure 12. Average surface friction coefficient for different volume fractions (0% and 6%), angles of attack, and Reynolds numbers (5-40).

5.9. Dimensionless Temperature Distribution

Figure 13 depicts the dimensionless temperature distribution in the central line of the flow for various volume fractions (0%-6%) of solid nanoparticles, angles of attack and Reynolds numbers. In the graphs of Figure 12, the dimensionless temperature changes in the central line of the flow and the fluid-surface temperature difference cause a layered heat transfer to the central zones of the flow. On the other hand, the presence of solid NPs enhanced the thermal conductivity of the cooling fluid. Among the analyzed graphs, the steps created on the graph are due to rows 1, 2 and 3. Hence, the growth of the dimensionless temperature can be attributed to the heat exchange between the primary tube bank and the third one. As

the fluid advances, more heat is absorbed from the environment, increasing the temperature in all zones, especially the central line zone of the flow. In all graphs, the dimensionless temperature decreased with enhancement of the Reynolds number. The temperature gradients decreased in lower Reynolds numbers, elevating the heating capacity of the flow between the tubes. The dimensionless temperature is maximized at low Reynolds numbers due to the slower velocity of the fluid and the spread of heat in all layers and the flow behavior approaching the temperature developed state. A rise in the angle of attack leads to more mixing and disruption of the flow and heat distribution among the layers above the hot surface, hence the highest value of the graphs is related to the angle of 90° whereas the lowest value belongs to the angle of 30°.
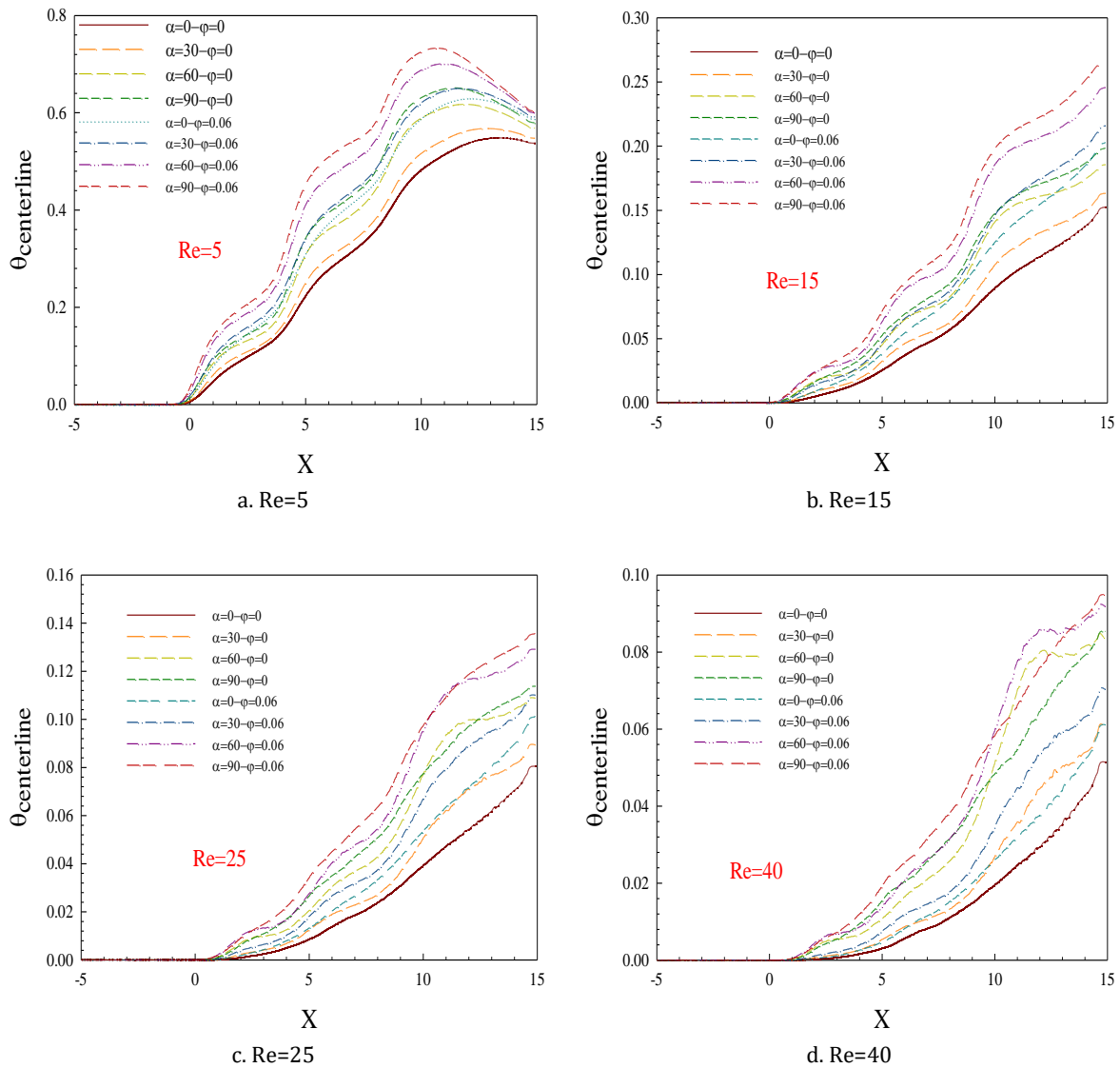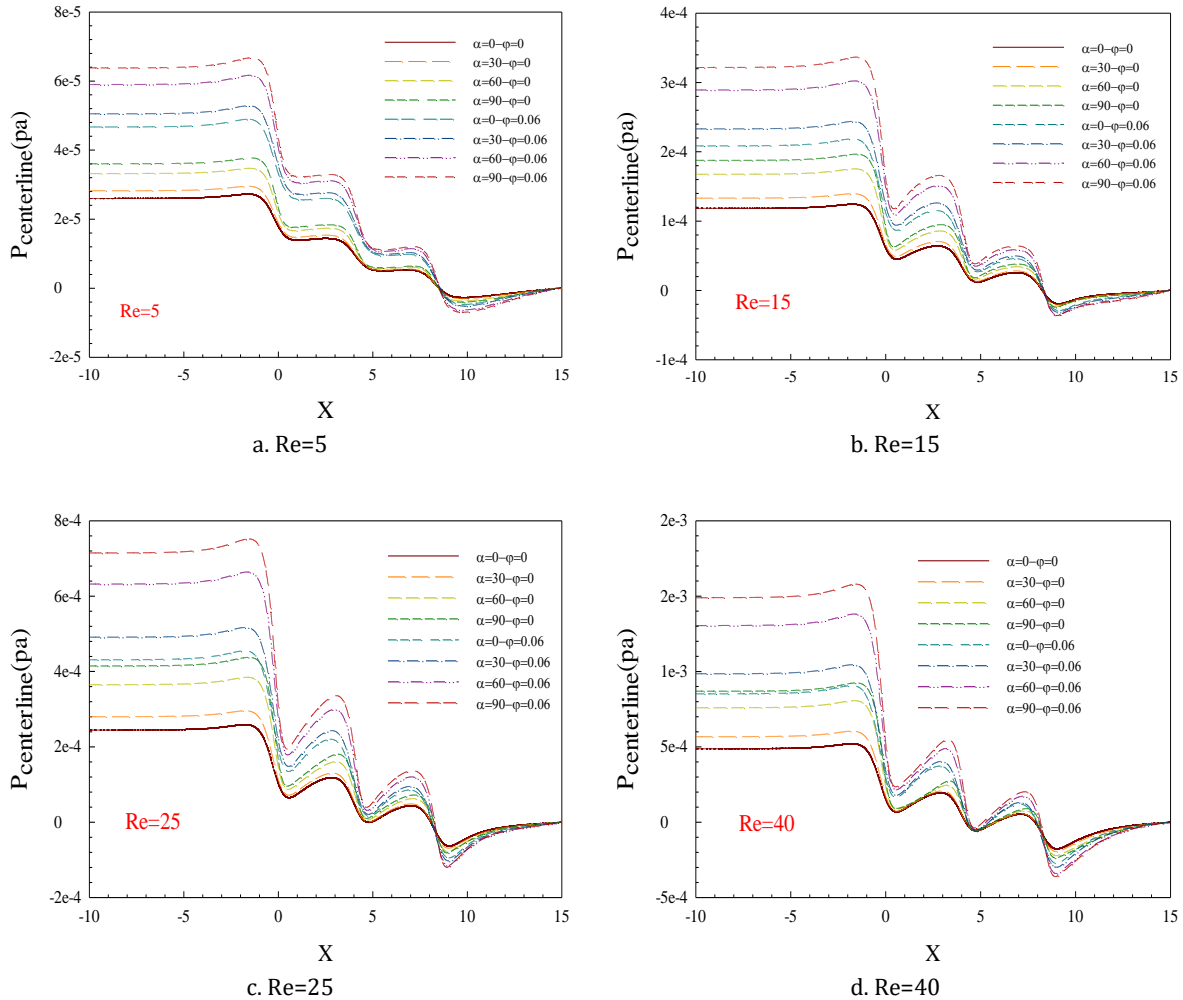

a. Re=5

b. Re=15

c. Re=25

d. Re=40

Figure 13. Dimensionless temperature distribution in the centerline of the flow for various solid NPs volume fractions (0%-6%), angles of attack, and Reynolds numbers

5.10.   Static Pressure Distribution

Figure 14 presents the static pressure distribution in the central line of the flow for different NPs volume fractions (0%-6%) and Reynolds numbers (5, 15, 25, and 40). This figure also shows the changes in static pressure drop on the central line of the flow. The steps on the graphs are caused by the impact of the flow with the tube banks, whose effects are layer by layer transferred to the central line of the flow. The presence of solid nanoparticles raises the fluid viscosity and

density, leading to a higher pressure drop along the path as heavier fluid requires greater depreciation and higher momentum to move. Also, the pressure drop and the momentum depreciation will be enhanced by raising the Reynolds number. Along the flow path, the smooth zone corresponds to the flow input area until the collision with the first tube banks. In the next tube banks, the pressure drop is declined as the fluid collides the tube banks at a lower velocity. Finally, the pressure drop tends to zero or discharges to the outside environment.

Figure 14. Static pressure distribution in the centerline of the flow for different NPs volume fractions (0%-6%), angles of attack, and Reynolds numbers.

Conclusions

This numerical research investigates the laminar flow of water/alumina nanofluid in a special shell-and-tube heat exchanger considering different NPs volume fractions and different Reynolds numbers.

The results show that an increase in the velocity of flow enhances the heat transfer coefficient, resulting in a more uniform temperature distribution. In addition, changes of angle of attack can leads to a higher velocity of the fluid flow between the tubes. More remarkable entropy reduction is observed with increasing

nanoparticle volume fraction at higher Reynolds numbers, Solid nanoparticles at a constant Reynolds number amplifies the flow velocity components and reduces the temperature gradient.

The Nusselt number can increase up to 17% at lower Reynolds number (Re = 5), which is up to 23% for higher Reynolds (Re = 40). Shell-side friction coefficient increases by 25 to 35% for Re = 5 and 40. For all cases, nanofluid volume fractions is more effective to increase/decrease the friction coefficient than angle of attack.

Nomenclature

Cp	Specific heat capacity (J/kg.K)
dp	Solid nanoparticle diameter (nm)
D	Elliptical tube equivalent diameter (m)
Gr	Grashof number
K	Thermal conductivity coefficient (W/m.K)
L_{us}	Input Length (m)
L_{tb}	Middle length (m)
L_{ds}	Output length (m)
S	Entropy (J/kg.K)
NPs	Nanoparticles
Nu_{ave}	Average Nusselt number
P	Pressure (pa)
Pr	Prandtl number
q″	Uniform heat flux (W/m^2)
Re	Reynolds number
y	Vertical coordinates
T	Temperature (K)
h	Convective heat transfer coefficient (W/m^2.K)
T_W	Wall temperature (K)
u_{in}	Input velocity (m/s)
U	Dimensionless horizontal velocity (U u/u$_i$)
v	Vertical velocity (m/s)
x	Horizontal coordinate (m)
X	Dimensionless horizontal coordinates (X x/D).

Greek Symbol

ρ	Density (kg/m^3)
β	Thermal expansion coefficient (1/K)
φ	Volumetric fraction of solid nanoparticles (%)
μ	Viscosity (pa.s)
θ	Dimensionless temperature
α	Angle (deg)

Conflicts of Interest

On behalf of all authors, the corresponding author states that there is no conflict of interest.

References

[1] Bahiraei, M., Rahmani, R., Yaghoobi, A., Khodabandeh, E., Mashayekhi, R., Amani, M., 2018. Recent research contributions concerning use of nanofluids in heat exchangers: A critical review. Applied Thermal Engineering, doi: https: //doi.org/10.1016/j. applthermaleng. 2018.01.041.

[2] Khanmohammadi, S., Rahimi, Z., Khanmohammadi, S., & Afrand, M., 2019. Triple-objective optimization of a double-tube heat exchanger with elliptic cross section in the presence TiO$_2$ nanofluid, Journal of Thermal Analysis and Calorimetry. doi.org/10.1007/s10973-019-08744-1.

[3] Tang, S. Z., Wang, F. L., He, Y. L., Yu, Y., and Tong, Z. X., 2019. Parametric optimization of H-type finned tube with longitudinal vortex generators by response surface model and genetic algorithm, Applied Energy, 239, 908–918.

[4] Zhao, L., Wang, B., Wang, R., and Yang, Z, 2019. Aero-thermal behavior and performance optimization of rectangular finned elliptical heat exchangers with different tube arrangements, International Journal of Heat and Mass Transfer. 133, 1196–1218.

[5] Deepakkumar, R., and Jayavel, S., 2017, Air side performance of finned-tube heat exchanger with combination of circular and elliptical tubes, Applied Thermal Engineering, 119, 360–372.

[6] Saffarian, M.R., Fazelpour, F. & Sham, M., 2019. Numerical study of shell and tube heat exchanger with different cross-section tubes and combined tubes. Int J Energy Environ Eng, 10, 33–46. https://doi.org/10.1007/s40095-019-0297-9.

[7] Mangrulkar, C.K., Dhoble, A.S., Deshmukh, A.R., 2016. Mandavgane, S.A., Numerical investigation of heat transfer and friction factor characteristics from in-line cam shaped tube bank in crossflow, Applied Thermal Engineering, doi:/10.1016/j.applthermaleng.2016.08.174.

[8] Wu, C. C., Chen, C. K., Yang, Y. T., and Huang, K. H., 2018. Numerical simulation of turbulent flow forced convection in a twisted elliptical tube, International Journal of Thermal Sciences, 132, 199–208.

[9] Etaig, S., Gamal., H., 2018. Numerical Investigation on the Laminar Flow in a Vertical Pipe with Elliptic Cross Section, International Journal of Science and Research (IJSR). 9(1), 1588-1592.

[10] Lu, G., and Zhai, X., 2018. Analysis on heat transfer and pressure drop of fin-and-oval-tube heat exchangers with tear-drop delta vortex generators, International Journal of Heat and Mass Transfer, 127, 1054–1063.

[11] Akbari, O.A., Goodarzi, M., Safaei, M. R., zarringhalam, M., Ahmadi Sheikh Shabani, G. A., and Dahari, M., 2016. A Modified Two-Phase Mixture Model of Nanofluid flow and Heat Transfer in 3-D Curved Microtube, Advanced Powder Technology, 27(5), 2175-2185.

[12] Mousavi, S.M., Akbari, O.A., Sheikhzadeh, Gh., Marzban, A., Toghraie, D., Chamkha, A.J., 2020. Two-phase modeling of nanofluid forced convection in different arrangements of elliptical tube banks, International Journal of Numerical Methods for Heat & Fluid Flow, 30(4), 1937-1966.

[13] Liu, H. L., Fan, C. C., He, Y. L., and Nobes, D.S., 2019. Heat transfer and flow characteristics in a rectangular channel with combined delta winglet inserts, International Journal of Heat and Mass Transfer, 134, 149–165.

[14] Mangrulkar, C. K., Dhoble, A. S., Chakrabarty, S. G., and Wankhede, U. S., 2017. Experimental and CFD

prediction of heat transfer and friction factor haracteristics in cross flow tube bank with integral splitter plate, International Journal of Heat and Mass Transfer, 104, 964–978.

[15] Abbasian Arani, A. A., Uosofvand, H., 2021. Double-pass shell-and-tube heat exchanger performance enhancement with new combined baffle and elliptical tube bundle arrangement, International Journal of Thermal Sciences, 167, 1145-1150.

[16] Pourfattah, F., Motamedian, M., Sheikhzadeh, G. A., Toghraie, D., and Akbari, O. A., 2017. The numerical investigation of angle of attack of inclined rectangular rib on the turbulent heat transfer of Water-Al2O3 nanofluid in a tube, International Journal of Mechanical Sciences, 131–132, 1106-1116.

[17] Jaferian, V., Toghraie, D., Pourfattah, F., Akbari, O. A., Talebizadehsardari, P., 2020. Numerical investigation of the effect of water/Al$_2$O$_3$ nanofluid on heat transfer in trapezoidal, sinusoidal and stepped microchannels, International Journal of Numerical Methods for Heat & Fluid Flow, 30 (5), 2439-2465.

[18] Yousefzadeh, S., Esmaeili, S., Eivazkhani, B., Akbari, O. A., Montazerifar, F., Toghraie, D., 2022. Numerical study of natural convection of nanofluid in a rectangular closed enclosure (RCE) affected by hot and cold flow in a two-layer microchannel. J Braz. Soc. Mech. Sci. Eng, 44, 197. https://doi.org/10.1007/s40430-022-03499-7.

[19] Fakour, M., Vahabzadeh, A., Ganji, D. D., 2015. Study of heat transfer and flow of nanofluid in permeable channel in the presence of magnetic field, Propulsion and Power Research. 4 (1), 50–62.

[20] Pak, B.C., and Cho, Y, I., 1998. Hydrodynamic and heat transfer study of dispersed fluids with submicron metallic oxide particles, Exp Heat Transfer, 11, 151–170.

[21] Brinkman, H. C., 1952. The viscosity of concentrated suspensions and solutions, J. Chem. Phys, 20, 571–581.

[22] Xuan, Y., Roetzel, W., 2000. Conceptions for heat transfer correlation of nanofluids, Int J. Heat Mass Transfer, 43, 3701–3707.

[23] Patel, H. E., Sundararajan, T., Pradeep, T., Dasgupta, A., Dasgupta, N., Das, S. K,. 2005. A micro-convection model for thermal conductivity of nanofluids. Pramana J Phys, 65(5), 863–869.

[24] Vanaki, S. M., Ganesan, P., Mohammed, H.A., 2016. Numerical study of convective heat transfer of nanofluids: a review, Renew Sustain Energy Rev. 54, 1212–39.

[25] Nimmagadda, R., Venkatasubbaiah, K., 2015. Conjugate heat transfer analysis of micro-channel using novel hybrid nanofluids (Al2O3+Ag/water). Eur J Mech B Fluids, 52,19–27.

[26] Pourfattah, F., Akbari, O. A., Jafrian, V., Toghraie, D., & Pourfattah, E., 2019. Numerical simulation of turbulent flow and forced heat transfer of water/CuO nanofluid inside a horizontal dimpled fin. Journal of Thermal Analysis and Calorimetry. doi:10.1007/s10973-019-08752-1.

[27] Zhang, H., Nie, X., Bokov, D. O., Toghraie, D., Akbari, O. A., Montazerifar, F., Pourfattah F., Esmaeili, Y., Khodaparast, R., 2022. Numerical study of mixed convection and entropy generation of Water-Ag nanofluid filled semi-elliptic lid-driven cavity, Alexandria Engineering Journal, 61(12), 11019-11030.

[28] Zhou, X. R., Wang, Y., Zheng, K and Huang, H., 2019. Comparison of heat transfer performance of ZnO-PG, α-Al2O3-PG, and γ-Al2O3-PG nanofluids in car radiator, Nanomaterials and Nanotechnology, 9, 1–12.

[29] Tavakoli, M. R., Akbari, O. A., Mohammadian, A., Khodabandeh, E., Pourfattah, F., 2019. Numerical study of mixed convection heat transfer inside a vertical microchannel with two-phase approach, Journal of Thermal Analysis and Calorimetry, 135 (2), 1119-1134.

[30] Ebrahimi, D., Yousefzadeh, Sh., Akbari, O. A., 2021. Montazerifar, F., Rozati, S. A., Nakhjavani, Sh., Safaei, M.R., Mixed convection heat transfer of a nanofluid in a closed elbow-shaped cavity (CESC), Journal of Thermal Analysis and Calorimetry, 144 (6), 2295-2316.

[31] Sarlak, R., Abed, A. M., Akbari, O. A., Marzban, A., Baghaei, Sh., Bayat, M., 2023. Numerical investigation of natural convection heat transfer of water/SWCNT nanofluid flow in a triangular cavity with cold fluid injection, Progress in Nuclear Energy, 155, 104513.

[32] Mir, S., Abed, A. M., Akbari, O. A., Mohammadian, A., Toghraie, D., Marzban, A., Mir, S., Montazerifar, F., Bemani, R., Smaisim, Gh. F., 2022, Effects of curvature existence, adding of nanoparticles and changing the circular minichannel shape on behavior of two-phase laminar mixed convection of Ag/water nanofluid, Alexandria Eng. J., https://doi.org/10.1016/j.aej.2022.10.059.

[33] Akcay, S., Akdag, U., 2022. Numerical analysis of thermal and hydraulic performance of pulsating nanofluid flow over cam-shaped tube bundles. Iranian Journal of Science and Technology Transactions of Mechanical Engineering, https://doi.org/10.1007/s40997-022-00572-3.

[34] Toolthaisong, S,. Kasayapanand, N., 2013. Effect of attack angles on air side thermal and pressure drop of the crossflow heat exchangers with staggered tube arrangement. Energy Procedia, 34, 417–29. https://doi:10.1016/j.egypro.2013.06.770.

[35] Salehi Afshar, K., Mirabdolah Lavasani, A., Abolfathi, S., Mobedi, P., 2022. The angle of attack effect on thermal-hydraulic performance of a cam-shaped tube with constant heat flux in crossflow. Experimental Heat Transfer, 10. http://doi.org/10.1080/08916152.2022.2059595.